

## Nucleation and hysteresis of vapor-liquid phase transitions in confined spaces: Effects of fluid-wall interaction

Yumei Men,<sup>1</sup> Qingzhao Yan,<sup>2</sup> Guangfeng Jiang,<sup>2</sup> Xianren Zhang,<sup>1</sup> and Wenchuan Wang<sup>1</sup>

<sup>1</sup>*Division of Molecular and Materials Simulation, Key Laboratory for Nanomaterials, Ministry of Education, Beijing University of Chemical Technology, Beijing 100029, China*

<sup>2</sup>*Department of Mathematics, Beijing University of Chemical Technology, Beijing 100029, China*

(Received 12 December 2008; revised manuscript received 24 February 2009; published 5 May 2009)

In this work, we propose a method to stabilize a nucleus in the framework of lattice density-functional theory (LDFT) by imposing a suitable constraint. Using this method, the shape of critical nucleus and height of the nucleation barrier can be determined without using a predefined nucleus as input. As an application of this method, we study the nucleation behavior of vapor-liquid transition in nanosquare pores with infinite length and relate the observed hysteresis loop on an adsorption isotherm to the nucleation mechanism. According to the dependence of hysteresis and the nucleation mechanism on the fluid-wall interaction,  $w$ , in this work, we have classified  $w$  into three regions ( $w > 0.9$ ,  $0.1 \leq w \leq 0.9$ , and  $w < 0.1$ ), which are denoted as strongly, moderately, and weakly attractive fluid-wall interaction, respectively. The dependence of hysteresis on the fluid-wall interaction is interpreted by the different nucleation mechanisms. Our constrained LDFT calculations also show that the different transition paths may induce different nucleation behaviors. The transition path dependence should be considered if morphological transition of nuclei exists during a nucleation process.

DOI: [10.1103/PhysRevE.79.051602](https://doi.org/10.1103/PhysRevE.79.051602)

PACS number(s): 64.60.qe, 64.70.fm, 68.43.Mn, 02.60.Gf

### I. INTRODUCTION

On the classical nucleation theory (CNT), embryos (bubble, droplet, or crystallite) of a new phase are always generated first before a first-order phase transition occurs [1]. To make a transition from an initial metastable state to a lower-energy one, the embryos have to overcome a free energy barrier. Taking the liquid-to-vapor phase transition as an example, a small bubble can appear in the metastable liquid because of the spontaneous fluctuations. If the bubble is small enough, it will collapse back into the liquid state. However, when the bubble exceeds a critical size and overcomes the nucleation free energy barrier, it will grow to a macroscopic size and lead to the liquid-to-vapor phase transition. In this intuitive picture, the embryo can be regarded as the pioneer of a new phase, i.e., nucleus. The nucleus with the critical size is called the critical nucleus. For the occurrence of a first-order phase transition, a critical nucleus of the new phase must be generated. In the framework of CNT, the nucleation barrier, which depends only on the size of the nucleus, is determined by a balance between the surface and volume free energies. As the simplest thermodynamics approach, CNT has been used for decades to answer nucleation problems in many areas.

For lack of knowledge on the microscopic structure of the critical nucleus, the CNT assumes that the material at the center of the nucleus behaves like a new phase in the bulk solution, and the surface of a small cluster is the same as that of an infinite planar surface. Both the assumptions become questionable when the nuclei are small enough to deviate from those in the bulk phase, and when their interfaces are sharply curved. In recent years, a number of computer simulation techniques, such as grand canonical Monte Carlo (MC) simulation, molecular dynamics (MD) simulation, nonequilibrium lattice fluids, density-functional theory

(DFT) and lattice density-functional theory (LDFT) have been developed to study phase transition processes and nucleation behaviors [1–17]. The nucleation theory based on the computer simulation techniques improves the unrealistic approximations in the CNT. For instance, Oxtoby and Evans [2] developed a nonclassical theory for the homogenous nucleation of the gas-liquid phase transition, by taking the free energy as a function of the actual density profile rather than a single parameter of the droplet radius.

Recently, nucleation behaviors in confined spaces have also drawn a lot of attention from both experimental and theoretical researchers [18,19]. One important reason is that nucleation plays an important role in the processes of adsorption and desorption of fluids in nanopores. In addition, nucleation behavior can also help us to understand adsorption hysteresis profoundly. In the adsorption science, hysteresis is a general feature that has been observed on the adsorption isotherms in mesoporous materials [20–25]. In the original works of using mean-field theory to study adsorption in open pores, Marconi and Swol [20,21] investigated the effects of pore ends on hysteresis. Very recently, Monson [25] applied mean-field kinetic theory to study the dynamics associated with capillary condensation and accompanying hysteresis. Bah *et al.* [26] proposed that hysteresis is related to nucleation difficulties, but the detailed relationship remains unsolved. Everett and Haynes [18] suggested that the liquid nucleation in a prewetted pore starts from a bump-like undulation, which grows into a bridge bounded by two hemispherical menisci. The bridge grows continuously until the pore is filled completely by the condensed fluid. Especially, they concluded that the critical nucleus of capillary condensation is the bump-like undulation rather than the liquid bridge.

The above-mentioned computer simulation techniques developed for bulk solutions are also applicable to investigate

the nucleation mechanism for the condensation and evaporation transitions of confined fluids and have achieved significant advances. For example, by using the MC method, Page and Sear [27] studied heterogeneous nucleation in and out pores. Vishnyakoy and Neimark [28–30] explored nucleation of liquid bridges and bubbles during condensation and evaporation of the Lennard-Jones fluid in cylindrical and spherical pores with MC simulations. Talanquer and his co-workers applied the DFT for the nucleation in slit pores [31] and cylindrical capillary [32]. Woo *et al.* [33] studied the nucleation mechanism of fluids desorption from disordered pore with MC simulations. Ustinov and Do [34] studied the nucleation in infinite cylindrical pore by two-dimensional DFT. Bolhuis and Chandler [35] combined the transition path sampling method [36,37] with molecular dynamics and Monte Carlo simulations to study the drying transition path in narrow pores. Although above works, as the best knowledge of us, no systematic work has been performed to investigate the effects of fluid-wall interactions on the nucleation behaviors.

DFT method is an effective tool to study nucleation behaviors of confined fluids. However, the application of DFT in an open system, it need predefined nuclei as input, which may introduce an uncontrollable source of uncertainty. When DFT is applied in a closed system, such as canonical ensemble, it is often difficult to judge whether the obtained nucleus is critical one or not, and the calculated results may suffer from finite-size effects [38]. Therefore, the aim of this work is to develop a method in the framework of DFT to study the nucleation behaviors in an open system while without using predefined nuclei as input. The proposed method is then used to study the dependence of nucleation behavior of porous systems on the fluid-wall interaction. In Sec. II, we give a simple description of the model and the method. Especially, we proposed a constrained method to stabilize a nucleus in the frame work of LDFT, and then to determine the shape of critical nucleus and its nucleation barrier. In Sec. III, we first use the mean-field LDFT to study the characteristics of hysteresis for simple fluids confined in infinitely long square-shaped nanopores. According to the dependence of hysteresis on the fluid-wall interaction, the fluid-wall interactions are classified into three regions, which are denoted by strongly, weakly, and moderately attractive fluid-wall interaction, respectively. Then, using the constrained DFT we discuss the different nucleation mechanisms for the condensation transition on adsorption branch and evaporation transition on desorption branch in the three different cases. In the final section, a brief summary of our work is addressed.

## II. MODEL AND METHODS

In our work, we discretize the space by employing a simple cubic lattice model [39]. Each lattice site can be empty or be occupied by a single fluid molecule or by the wall. The fluid and wall occupancy variables are denoted by  $\tau_i=0, 1$  and  $(1-\eta_i)=0, 1$  respectively. The fluid molecule on

site  $i$  only interacts with its neighbors on the six nearest sites. The interactions of fluid-fluid and fluid-wall are expressed by  $w_{ff}$  and  $w_{mf}$ , respectively. The ratio of the fluid-wall over the fluid-fluid interaction ( $w=w_{mf}/w_{ff}$ ), describes the “wettability.”  $w>1$  indicates that the interaction between the pore wall and fluid is stronger than that between the fluid molecules, and  $0<w<1$  represents the fluid-wall interaction is weaker. In our calculations, all the quantities used are dimensionless. The reduced temperature  $T^*$  and the chemical potential  $\mu^*$  are defined as  $T^*=k_B T/w_{ff}$  and  $\mu^*=\mu/w_{ff}$ , respectively. For all our calculations, the temperature of  $T^*$  was set to 0.8, and the volume of the simulation box was selected as  $V=40\times 40\times 60$ . To represent the infinitely long pore with a square shape, the periodic boundary condition was applied in  $z$  direction. With no specification, the width of the square pore,  $R_B$ , was fixed at 20.

In classical DFT, Helmholtz energy functional, designated as  $F[\rho_i]$ , is often referred to as the intrinsic Helmholtz energy, meaning that it is an inherent property of the system and is independent of the external potential. Our model is defined by the Helmholtz energy proposed by Kierlik *et al.* [39] to describe a confined inhomogeneous fluid with fixed overall density in the system,

$$F(\{\eta_i\}) = \frac{1}{\beta} \sum_i [\rho_i \ln \rho_i + (\eta_i - \rho_i) \ln (\eta_i - \rho_i)] - w_{ff} \sum_{\langle ij \rangle} \rho_i \rho_j - w_{mf} \sum_{\langle ij \rangle} [\rho_i (1 - \eta_j) + \rho_j (1 - \eta_i)]. \quad (1)$$

Note that Kierlik *et al.* [40] pointed out that there is symmetry  $w \leftrightarrow 1-w$  for Eq. (1). The symmetry allows one to restrict the study to  $w>0.5$  or  $w<0.5$ , as is illustrated for instance by Porcheron and Monson [41] in their study of mercury porosimetry. In this work, to model the some porous media with strong adsorptive abilities, we consider the range of  $2.5>w>0.0$ . Our work does confirm that the nucleation behavior satisfies the symmetry requirement of property for  $w \leftrightarrow 1-w$  within the calculation uncertainty.

For a confined inhomogeneous fluid in contact with an external reservoir, the formulation of grand potential can be expressed though the Legendre transform

$$\Omega(\{\eta_i\}) = F(\{\eta_i\}) - \mu \sum_i \rho_i. \quad (2)$$

The local density at site  $i$  is determined by the partial derivative of the grand potential with respect to the intrinsic chemical potential:

$$\rho_i = - \left( \frac{\partial \Omega}{\partial (\mu - v_i)} \right)_{T,V}, \quad (3)$$

where  $v_i = -w_{mf} \sum_j' (1 - \eta_j)$  is the external field on site  $i$ . At equilibrium, the grand potential  $\Omega$  of the adsorbed fluid is minimized to give the equation for the equilibrium density profile  $\rho_i$ ,

$$\frac{\partial \Omega[\rho]}{\partial \rho} = 0. \quad (4)$$

The corresponding equation for the fluid density on each site is

$$\rho_i = \frac{\eta_i}{1 + \exp\left\{-\beta\left[\mu + \sum_{j \neq i} [w_{\text{ff}}\rho_j + w_{\text{mf}}(1 - \eta_j)]\right]\right\}}. \quad (5)$$

The above set of nonlinear coupled equations can be solved by the classical successive substitution scheme [39,42].

According to the classical nucleation theory, first-order phase transitions are initiated by spontaneous appearance of nuclei from a metastable state. If the size of a nucleus exceeds a critical one and has overcome a free energy barrier, it will grow and lead to phase transition spontaneously. In this work, we attempted to find out the critical nucleus and calculate the nucleation barrier in grand canonical ensemble at a given chemical potential and temperature.

In studying an activated process, such as nucleation, we need to know not only the free energy of the stable or metastable state, but also the properties of the transition states, which correspond to saddle points of free energy functionals. Although finding a saddle point of a functional poses a serious numerical problem, in some cases one can identify the unstable directions of the functional and stabilize it by applying a suitable constraint. For example, Auer and Frenkel [8,9] used a bias potential to control the size of the nucleus in their Monte Carlo method to study crystal nucleation. In-

spired by their works, in this work we stabilize a nucleus with a suitable constraint. As a result, the morphology and energy barrier for critical nuclei can be determined subsequently. Here we use liquid-to-vapor phase transition as an example to describe our scheme for searching the shape and energy barrier for critical nuclei.

To impose the constraint, we employ a Lagrange multiplier  $\frac{1}{2}\kappa(\Psi - \Psi_0)^2$  in the corresponding grand potential expression. In the term,  $\Psi$  is an order parameter defined as the number of vapor sites in the system (with density less than 0.5), while  $\Psi_0$  is the target number of vapor sites and  $\kappa$  is the Lagrange multiplier. Note that  $\Psi \equiv \sum_i \eta_i \chi_i$ , where  $\chi_i$  is equal to 1 when site  $i$  is not occupied by the matrix and its local density is less than 0.5. Otherwise,  $\chi_i$  is equal to 0. The constrained grand potential functional can then be given as

$$\begin{aligned} \Omega_0(\{\rho_i\}) = & \frac{1}{\beta} \sum_i [\rho_i \ln \rho_i + (\eta_i - \rho_i) \ln(\eta_i - \rho_i)] - w_{\text{ff}} \sum_{\langle ij \rangle} \rho_i \rho_j \\ & - w_{\text{mf}} \sum_{\langle ij \rangle} [\rho_i(1 - \eta_j) + \rho_j(1 - \eta_i)] - \mu \sum_i \rho_i \\ & + \frac{1}{2} \kappa \left( \sum_i \eta_i \chi_i - \Psi_0 \right)^2. \end{aligned} \quad (6)$$

The local density at site  $i$ ,  $\rho_i$ , is determined by minimizing the constrained grand potential, namely  $\frac{\partial \Omega_0[\rho]}{\partial \rho} = 0$ . The corresponding equations for the fluid density on each site are

$$\rho_i = \frac{\eta_i}{1 + \exp\left\{-\beta\left[\mu + \sum_{j \neq i} [w_{\text{ff}}\rho_j + w_{\text{mf}}(1 - \eta_j)]\right] + \kappa \eta_i \left(\sum_i \eta_i \chi_i - \Psi_0\right) \delta(\rho_i - 0.5)\right\}} \quad (7a)$$

in which  $\delta$  represents Dirac delta function. In principle, based on Eq. (7a) the density profile for the system containing a nucleus of  $\Psi = \Psi_0$  can be solved in an iteration process using an initial density profile with random distribution of vapor sites. Therefore, the shape of the nucleus and its energy barrier can be determined by the constrained LDFT. Initially, several runs using this scheme were performed starting from random initial conditions, but this scheme could not consistently generate the lowest-free energy configuration for a given value of  $\Psi_0$ . Normally, the calculations generate configurations with several small nuclei instead of a large nucleus with the lowest global free energy. This is not surprising since the constrained LDFT simulations started from random initial conditions are frequently trapped in metastable states, and as a result the constrained LDFT with this scheme fail to generate the lowest-free energy configuration.

Based on above difficulty, we modified Eq. (7a) into two folds. On the one hand, to avoid the unstable numerical evolution caused by the Dirac delta function while remaining

the constraint, we replaced  $\kappa \eta_i (\sum_i \eta_i \chi_i - \Psi_0) \delta(\rho_i - 0.5)$  with  $\text{sgn}(\sum_i \eta_i \chi_i - \Psi_0)$ , where

$$\text{sgn}\left(\sum_i \eta_i \chi_i - \Psi_0\right) = \begin{cases} +1, & \left(\sum_i \eta_i \chi_i\right) - \Psi_0 > 0 \\ 0, & \left(\sum_i \eta_i \chi_i\right) - \Psi_0 = 0 \\ -1, & \left(\sum_i \eta_i \chi_i\right) - \Psi_0 < 0 \end{cases}.$$

On the other hand, to speed up the evolution of the nuclei from the metastable states (with several small nuclei in the constrained system) to the global lowest free energy states (a full developed nucleus), the sign function in Eq. (7a) is multiplied by  $[1 - \prod_{j \neq i} \chi_j - \prod_{j \neq i} (1 - \chi_j)]$ , where  $\prod_{j \neq i}$  means the product over all nearest neighbors of the site  $i$ . Obviously, for the site  $i$  on the liquid-vapor interface,  $[1 - \prod_{j \neq i} \chi_j - \prod_{j \neq i} (1 - \chi_j)]$  is equal to 1, otherwise it is equal to 0. It is equivalent to a potential energy forcing the number of sites

on the vapor-liquid interface to decrease. Hence, after the introduction of the  $[1 - \prod_{j \neq i} \chi_j - \prod_{j \neq i} (1 - \chi_j)]$ , the efficiency to find the global lowest free energy states in the constrained LDFT can be significantly speeded up. Note that both the

stable and metastable states in the constrained system may be unstable in an unconstrained system.

Therefore, the local density at site  $i$  is in fact determined from the following equation:

$$\rho_i = \frac{\eta_i}{1 + \exp\left\{-\beta\left[\mu + w_{\text{ff}} \sum_{j \neq i} \rho_j + w_{\text{mf}} \sum_{j \neq i} (1 - \eta_j) + \kappa \operatorname{sgn}\left(\sum_i \eta_i \chi_i - \Psi_0\right) \left[1 - \prod_{j \neq i} \chi_j - \prod_{j \neq i} (1 - \chi_j)\right]\right]\right\}}. \quad (7b)$$

In the above expression,  $\kappa \operatorname{sgn}(\sum_i \eta_i \chi_i - \Psi_0) [1 - \prod_{j \neq i} \chi_j - \prod_{j \neq i} (1 - \chi_j)]$  is equivalent to a potential exerted on the vapor-liquid interface to reduce the interface area while forcing the system to evolve with  $\operatorname{sgn}(\sum_i \eta_i \chi_i - \Psi_0) = 0$ . The Lagrange multiplier  $\kappa$  represents the strength of the force, which was set to be 1.0. At a given chemical potential, Eq. (7b) is solved in an iteration process. This method allows us to compute the energy barrier and the shape of nuclei as a function of the cluster size  $\Psi_0$ . Thus, the critical nucleus can be identified as the nucleus with the highest energy barrier.

The constrained method can be understood as follows. The constrained grand potential in our method is in fact the deviation potential named by Neimark and Vishnyakov [30]

$$W(N, V, T, \mu) = F(N, V, T) - N\mu, \quad (8)$$

where  $N$  [namely,  $\Psi \equiv \sum_i \eta_i \chi_i$  in Eq. (7b)] represents the number of particles in the constrained system. According to Neimark and Vishnyakov [30], it is the deviation potential that determines the probability to sample  $(N, V, T)$  state in grand canonical ensemble at a given chemical potential  $\mu$  and the unconstrained grand potential in an unconstrained grand canonical ensemble is given by

$$\Omega(\mu, V, T) = -kT \ln \sum_N \exp[-W(N, V, T, \mu)/kT]. \quad (9)$$

Obviously, the minima and maxima of the deviation potential with regard to  $N$  at a given chemical potential correspond respectively to the most and least probable states obtained from the unconstrained grand canonical ensemble. Thus, two minima of deviation potential  $W(N, V, T, \mu)$ , respectively, corresponds to the state and metastable states, while the maximum corresponds to the transient state and determines the nucleation barrier [30]. This is why we determine the critical nucleus as the nucleus with the highest energy barrier in our constrained method (see below).

The nucleation behavior is investigated in our constrained method by analyzing the constrained states  $(N, V, T, \mu)$ , very similar to the method in the framework of canonical ensemble. However, in comparison with canonical ensemble this method not only avoids the difficulty to calculate the chemical potential [30,32], but also significantly alleviates the finite-size effects encountered by canonical ensemble [38], because the chemical potential is given in advance.

### III. RESULTS AND DISCUSSION

#### A. Adsorption isotherms

As an application of this method, in the work we studied the effects of fluid-wall interaction on the nucleation behavior. First, we calculated adsorption isotherms of simple fluids in square-shaped nanopores with infinite length. A typical adsorption isotherm for  $R_B=20$ ,  $w=2.5$ , and  $T^*=0.8$  is presented in Fig. 1(a). The isotherm exhibits two hysteresis loops at different chemical potentials, which correspond to two different phase transitions, namely, layering transition and capillary condensation, respectively. The small loop represents the layering transition, while the main loop shows the vapor-liquid transition in the confined space. Here, we focus on the nucleation mechanism of the main loop.

To distinguish the stable and metastable states, the corresponding grand potential variation for the adsorption isotherm [43,44] [see Fig. 1(a)] is given in Fig. 1(b). As is shown in the picture, the chemical potential for the capillary coexistence is determined by the intersection point of the two grand potential curves, namely, where the branches of adsorption and desorption have the same grand potential value ( $\mu^* = -3.09$ ). In the low chemical potential region of the loop [see Fig. 1(a)], the vaporlike phase on the adsorption branch is stable, and the liquidlike phase on the desorption branch is metastable, because the grand potential of vaporlike phase is lower. However, when the chemical potential is higher than that for capillary coexistence, the liquidlike state becomes globally stable, while the vaporlike states become metastable [43]. The metastable adsorption branch of the main loop terminates at a vaporlike spinodal, while the metastable desorption branch terminates at a liquidlike spinodal.

Figure 2 presents several adsorption isotherms obtained for different pore widths and fluid-wall interactions. For comparison, the isotherms for vapor-to-liquid and liquid-to-vapor phase transition in the bulk solution are also given. It is found from Fig. 2 that the position of the small loop depends only on  $w$ , rather than the pore width. For the strongly attractive fluid-wall interaction, the small loop occurs before the large loop, which means that the prewetting film near the pore wall forms before the capillary condensation. As  $w$  decreases, the small loop shifts to the higher chemical potential and merges into the main one especially when  $w \leq 1$ . This observation is in good agreement with our previous works [43–46].

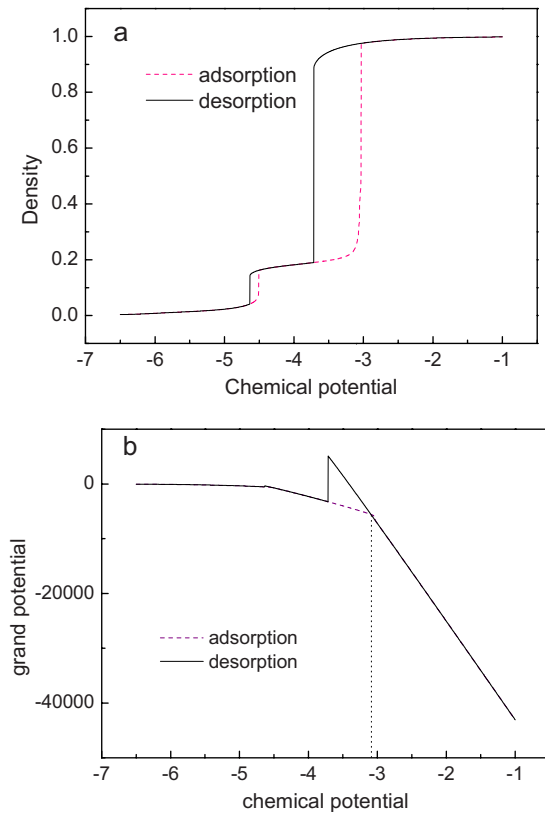


FIG. 1. (Color online) (a) Adsorption isotherm for the system with  $w=2.5$  and  $R_B=20$  at the temperature  $T^*=0.8$ . (b) Corresponding grand potentials for the adsorption isotherm in (a). The intersection point of the grand potential curves for the adsorption and desorption branches corresponds to the chemical potential for the capillary coexistence.

For the phase transitions in the main loop, it is found in Fig. 2(a) that if  $w > 0.9$  the chemical potentials for liquidlike spinodals are nearly identical for different pore widths and  $w$ . Moreover, they take the same position as the liquid spinodal of the bulk solution. However, if  $w$  is small enough ( $w \leq 0.1$ ), the vaporlike spinodals for the confined system occur at the same chemical potential for the bulk vapor spinodal, regardless of the value of the pore widths and the fluid-wall interactions [see Fig. 2(b)]. According to the characteristics of their adsorption isotherms, the liquid-wall interaction parameter,  $w$ , is classified into three regions, which are denoted as strongly ( $w > 0.9$ ), weakly ( $w < 0.1$ ) and moderately attractive fluid-wall interaction ( $0.1 \leq w \leq 0.9$ ), respectively.

Since a first-order phase transition proceeds with nucleation and growth, in this work we try to relate the adsorption characteristics, especially the position and width of hysteresis loops, to the nucleation mechanism. For example, to interpret the agreement between the liquidlike spinodals for the confined systems of  $w > 0.9$  and that for the bulk solution as well as the independence of spinodals on pore width and  $w$ , it is proposed here that the confined liquid-to-vapor (evaporation) transition on the desorption branch is initiated by the homogeneous nucleation of bubbles in the center of the pore, in a similar way as the homogeneous nucleation in

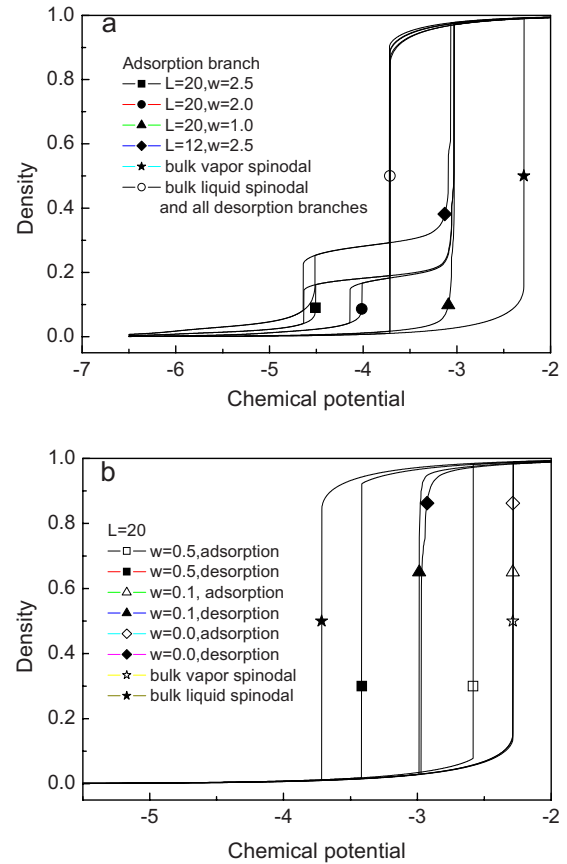


FIG. 2. (Color online) Dependence of the adsorption isotherms on pore width and fluid-wall interaction. (a) Adsorption isotherms for pore with  $R_B=20, 12$ , and  $w > 0.9$ . (b) Adsorption isotherms for  $w < 1.0$ . The isotherms for the bulk solution, which were similarly calculated by LDFT in the absence of pore walls, are also shown in the figure for comparison.

the bulk solution. As a result, the effects of the existence of the pore wall on evaporation are negligible. Similarly, for the systems with weak fluid-wall interactions, the confined vapor-to-liquid transition (condensation) on the adsorption branch is initiated from the nucleation of spherical droplets in the center of the pore. To verify our assumptions, we investigate the behaviors of nucleation, which is the precursor of a first-order phase transition.

### B. Determination of critical nucleus and nucleation barrier

To investigate the nucleation behaviors of the systems with strong fluid-wall interactions, we set  $w=2.5$  and search the critical nuclei for evaporation and condensation, respectively. We first take the nucleation of capillary evaporation at  $\mu = -3.2$  as an example to demonstrate the proposed scheme for searching the critical nucleus. With a given number of vapor sites,  $\Psi_0$ , the initial vapor sites (hence the initial density profile) were randomly inserted into a metastable liquid state [see Fig. 3(a)]. Then, using the iteration scheme of Eq. (7b), the unstable nucleus was stabilized due to the constraint (see Fig. 4). The distribution and the number of vapor sites were adjusted continually in the iteration process [see Figs.

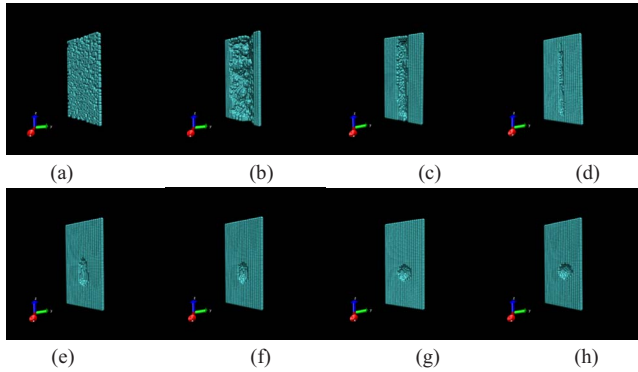


FIG. 3. (Color online) Typical snapshots generated in the iteration process with the different number of iteration steps. (a) Initial density profile with randomly distributed vapor sites. (b-d) The aggregation of vapor sites. (e-g) The evolution of the formed bubble. (h) The finally formed nucleus.

3(b) and 3(c)]. After several iteration steps, a bubble with irregular geometry formed and distinguishable vapor-liquid interface appeared [see Fig. 3(d)], while the constrained grand potential is still at a higher value. Further iteration step changes the position and the geometry of the bubble continuously [see Figs. 3(e) and 3(g)], and as a result, the corresponding grand potential decreases until it reaches its minimum. After sufficient number of iteration steps, the solution of nucleus reached the minimum of the constrained grand potential and a stable nucleus is formed, as is shown in Fig. 3(h). For different target sizes of nuclei formed from the initial metastable liquidlike state, the computed energy barriers are shown in Fig. 5(a). The energy barrier for a nucleus is estimated through the work of formation of the nucleus from its corresponding metastable state, which is equal to the difference between the constrained grand potential of the state and the grand potential of its corresponding unconstrained metastable state at the given chemical potential. The state on the top of the energy barrier corresponds to the critical nucleus.

Above iteration method initiated from a random density profile is sufficient if there is not morphological transition of nuclei during a nucleation process. If the morphological tran-

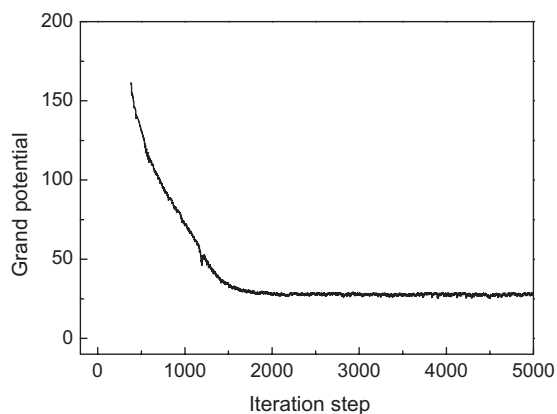


FIG. 4. Evaluation of the constrained grand potential in the process of iteration to form and stabilize a nucleus with a given size.

sition of nuclei exists, our calculations indicate that the different transition paths may induce different nucleation behaviors. In other words the nucleation behavior shows transition path dependence. To take into account the effect, in this work we consider two different transition paths. One nucleation transition path is obtained in a series of consecutive simulations with a monotonically increasing nucleus size in which the last configuration generated at each nucleus size serves as the initial configuration for the next run at increasing nucleus size. The other transition path, which first starts with a large nucleus, is contrarily obtained from a series of consecutive simulations with a monotonically decreasing nucleus size. Figure 5(b) shows an example of corresponding nucleation behaviors for the different transition paths. For the first path a small bump first forms and then grows as the nucleus size increases. When the bump structure reaches its stability limit [ $S_a$  in Fig. 5(b)] it becomes unstable and suddenly transforms into a bridge structure. In contrast, for the second transition path, the morphology of nucleus begins with a bridge structure and gradually decreases until a sudden morphological transition from bridge to bump occurs at turnover point  $S_b$ . Thus, if the nucleus size is in the range between  $S_a$  and  $S_b$ , the corresponding nucleus shape depends on the transition path and a hysteresis loop is formed. The intersection of the two transition paths, which corresponds to the same energy barrier for both bridge and bump structures, separate the stable bridge (and corresponding metastable bump) at large nucleus size and stable bump (metastable bridge) at small size. This pathway dependence of nucleus reminds us the adsorption hysteresis for adsorption in open system (for example, see Fig. 1). But it is worth noting that we are considering a constrained system and any nucleus from this system is unstable in an open system. The states  $S_a$  and  $S_b$  seemingly resemble the superspinodals named by Némárk and Vishnyakov [17,29], which represent the limit of stability of states sampled by means of the gauge cell Monte Carlo method [29].

As critical nuclei correspond to the local maxima of the grand thermodynamic potential with respect to density profile along the path of nucleus growth, thus for the case of Fig. 5(b) we set the turnover point from bump to bridge transition,  $S_a$ , as the critical nucleus. However, because the calculated nucleus is unstable in an open system and the bridge structure can be created with lower energy barrier [see Fig. 5(b)], it is also possible that the bump grows and spontaneously transforms into a bridge structure after its size is greater than that for the intersection. If this is correct, the critical nucleus would correspond to the intersection of the two pathways. The two methods to determine the nucleation behavior result in the same nucleus morphologies, but lead to different nucleation barriers. In this work we use the first method to determine the critical nucleus.

In Fig. 5(b), the critical nucleus locates at the boundary of the hysteresis loop of nucleus evolution due to the different transition paths. However, there are other cases where the critical nuclei formed before or after the hysteresis loop. Figures 5(c) and 5(d) show the two different cases, respectively. For these cases, the critical nuclei are undoubtedly determined according to the highest energy barrier.

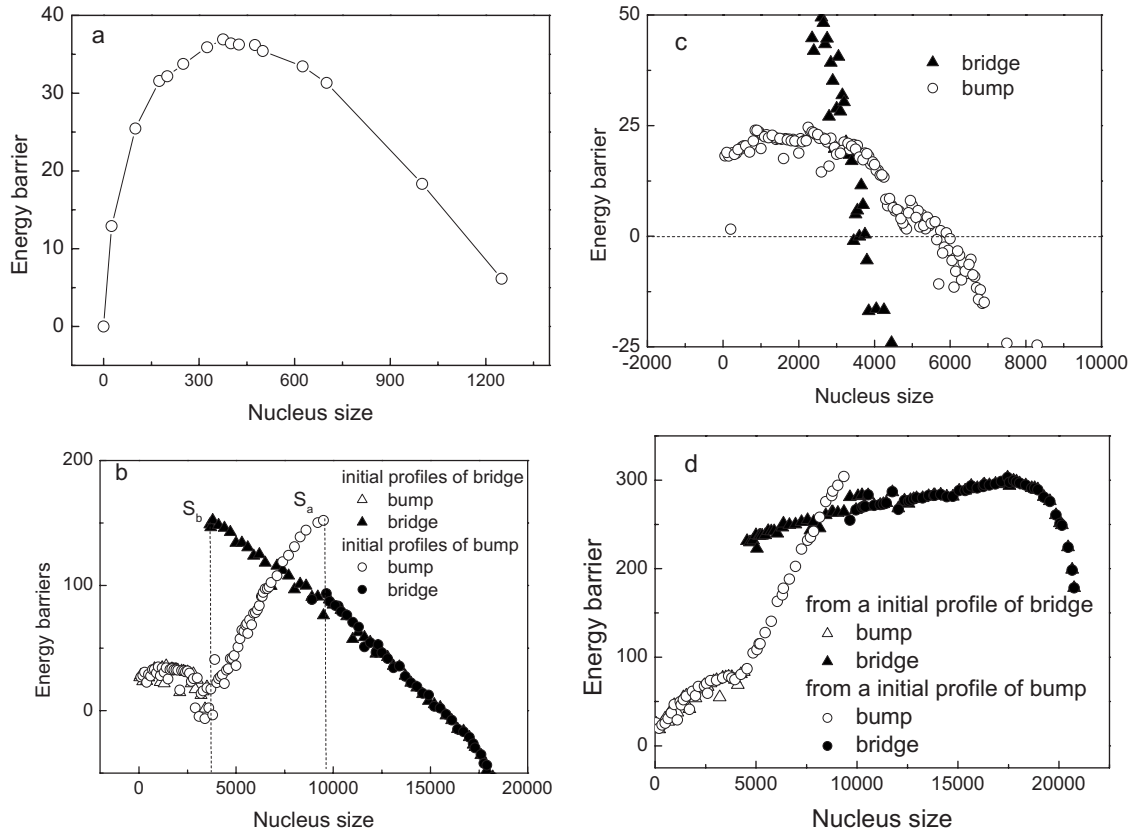


FIG. 5. The energy barrier associated with the formation of a cluster of size  $\Psi_0$ . The nucleus with highest energy barrier corresponds to the critical nucleus. (a) Nuclei of evaporation for  $w=2.5$  and  $\mu=-3.20$ . (b) Nuclei of condensation for  $w=2.5$  and  $\mu=-3.08$ . Here we set  $S_a$  as the critical nucleus. (c) Nuclei of condensation for  $w=2.5$  and  $\mu=-3.05$ . (d) Nuclei of condensation for  $w=2.5$  and  $\mu=-3.10$ . Note that in this case the energy barrier is calculated from the stable vaporlike state.

**C. Nucleation mechanism for strong fluid-wall interaction ( $w > 0.9$ )**

The nucleation behaviors for the system with strongly attractive fluid-wall interaction have been discussed in this section. We used  $w=2.5$  as an example. The obtained critical nuclei at four chemical potentials along desorption branch, namely,  $\mu=-3.10, -3.12, -3.16$  and  $-3.20$ , are shown in the first row of Fig. 6. It is found that a bubble in the center of the pore nucleates a new phase from the liquidlike metastable state. The critical nucleus exhibits a spherical shape, and the bubble size decreases with chemical potential. The obtained nucleation barriers at different supersaturation states also decreases monotonically with the decrease of the chemical potential, as is shown in Fig. 7(a). The nucleation barriers of capillary evaporation for the pore with  $R_B=12$  are also calculated, and they are identical with those for  $R_B=20$ . It is also found the nucleation barriers for evaporation in different pore sizes well agree with that for the bulk solution. The reason of the agreement is that a critical nucleus in the center of the pore would not be affected by the wall, as long as the nucleus is far from the wall. This is also the reason why evaporation on desorption branches for different value of  $w$  ( $w > 0.9$ ) and different pore widths take place at the same position as that of the bulk solution. We must note that an observable disagreement of nucleation barriers between confined fluid and bulk solution appears when the

chemical potential is close to the chemical potential of capillary coexistence. This is because at these states the critical nucleus in a confined space is no longer spherical due to the space confinement (see the snapshot for  $\mu=-3.10$  in Fig. 6), which results in the displacement from bulk solution.

To further prove the validity of our constrained LDFT, we also compare the results of nucleation in bulk solution with those by the method of Oxtoby and Evans [2]. The calculated nucleation barriers from the two different methods are com-

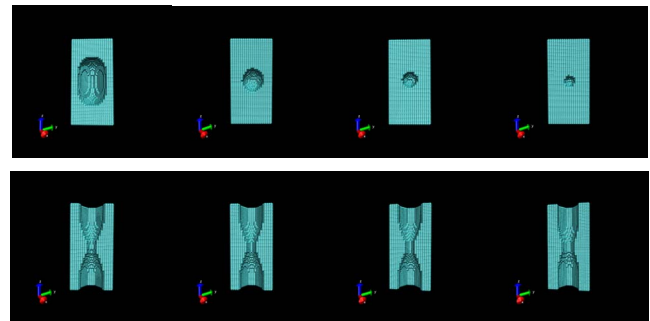


FIG. 6. (Color online) Calculated critical nuclei for  $w=2.5$ . The first row shows, from left to right, the morphologies of critical nuclei in desorption branch for  $\mu=-3.10, -3.12, -3.16$ , and  $-3.20$ , respectively. While the second row shows the morphologies of critical nuclei in adsorption branch for  $\mu=-3.08, -3.07, -3.06$ , and  $-3.05$ , respectively.

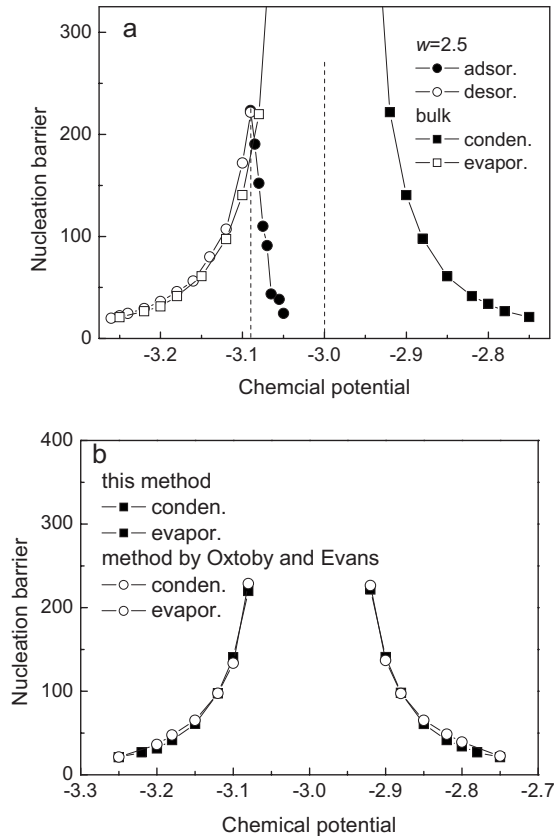


FIG. 7. (a) Comparison of the nucleation barriers of vapor-liquid transitions for a pore of  $R_B=20$  and those for bulk solution. The intersection point of two nucleation barrier curves for the confined system corresponds to the chemical potential for the capillary coexistence, which is in good agreement with that obtained from the adsorption isotherms [see Fig. 1(b)]. (b) Comparison of the nucleation barriers for vapor-liquid transitions in bulk solution calculated by this method and those by the method of Oxtoby and Evans [2].

pared in Fig. 7(b). The figure indicates that they are in good agreement.

Note that in this case of  $w > 0.9$  desorption for finite long pores with pore ends may show different nucleation mechanism, as comparison with infinitely long pores we studied here. The nucleation sites for desorption of finite pores still remains unclear. The pore ends or external surface of porous layer [23] may serve as the nucleation sites for desorption.

For the condensation transition on the adsorption branch, Fig. 2(a) shows that its position on the hysteresis loop significantly deviates from that for the bulk vapor-to-liquid transition, and differs for the different pore sizes. The difference indicates that there may exist a different nucleation mechanism of the condensation transition for  $w > 0.9$  in comparison with the bulk solution. To examine the difference of nucleation mechanisms, we also performed the constrained LDFT calculations for the nucleation of capillary condensation.

Typical density profiles of the critical nuclei at different chemical potentials, including  $\mu = -3.08$ ,  $-3.07$ ,  $-3.06$ , and  $-3.05$ , are shown in the second row of Fig. 6. Note that in this case, transition path dependence should be considered, as shown in Fig. 5(b). As one can see, the morphologies of

critical nuclei take the shape of annular bump at both high and low supersaturation states. The bump morphologies occurring near the pore wall are quite different from spherical nucleus occurs in the center of the pore. The difference is ascribed to the strong fluid-wall interaction, which results in the formation a fluid layer (prewetting film) on the wall before capillary condensation. The fluid layer plays an important role in adsorption in the pore. Different from the homogeneous nucleation in the bulk solution, the critical nuclei for condensation transitions are formed on the prewetting film. Hence the nucleation barrier for the nucleation via annular bump, as is shown in Fig. 7(a), can be substantially reduced in comparison with that for the vapor-to-liquid transition via spherical droplet in the bulk solution.

Above calculations show that the nucleation barrier for condensation decreases substantially in comparison with that for bulk solution, while the nucleation barrier for evaporation is nearly kept unchanged. As a result, the capillary coexistence, at which the two curves of nucleation barriers corresponding to adsorption and desorption branches intersect, shifts to a much lower chemical potential [see Fig. 7(a)]. Note that the point of intersection of the two curves of nucleation barriers [see Fig. 7(a)] corresponds to the chemical potential of capillary coexistence in the pore, which is in good agreement with that obtained from the adsorption isotherms [see Fig. 1(b)]. This proves the Maxwell rule that the point of intersection of the grand thermodynamic potentials determines the vapor-liquid equilibrium in the pore [28].

It is well known that the values of the chemical potentials for condensation and evaporation of confined fluids can differ significantly from their bulk ones. Our results indicate that the major reason for the difference is the change of the nucleation mechanism due to the existence of pore walls. In general, our calculations confirm the scenario of Everett and Haynes [18] for vapor condensation in a confined space that the critical nucleus of condensation is an annular bump, and the critical nucleus of evaporation is a bubble in the pore center. Our results also confirm that the hysteresis phenomenon of confined fluids originates from the difficulty of nucleation of a new phase. Moreover, in comparison with the phase transition in the bulk solution, our results demonstrate that the strong attraction due to the pore wall ( $w > 0.9$ ) causes the nucleation mechanism for capillary condensation changing from homogeneous to heterogeneous. The heterogeneous nucleation near the wall reduces the nucleation barrier substantially and makes the condensation take place at the lower chemical potentials. Hence, it is the fluid-wall interaction that induces the change of the nucleation mechanism, which then shifts the equilibrium phase transition and modifies the position and width of the hysteresis loop against its bulk counterpart.

#### D. Nucleation behavior for moderate ( $0.1 \leq w \leq 0.9$ ) and weak fluid-wall interaction ( $w < 0.1$ )

In this section, we considered the systems with moderately attractive fluid-wall interactions ( $0.1 \leq w \leq 0.9$ ). To investigate the dependence of the nucleation mechanism on the fluid-wall interactions, we considered several different val-

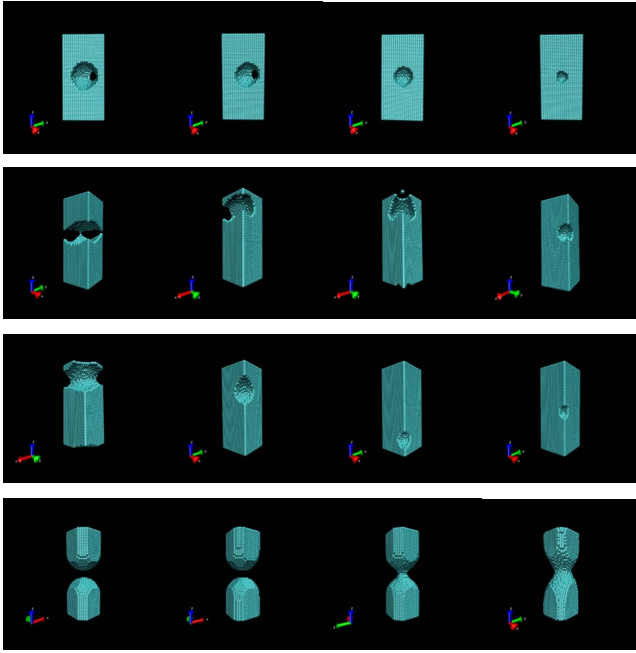


FIG. 8. (Color online) Morphologies of critical nuclei in desorption branches for different  $w$ . The first row:  $w=0.9$ , in which nuclei morphologies from left to right correspond to  $\mu=-3.08$ ,  $-3.10$ ,  $-3.12$ , and  $-3.14$ , respectively. The second row:  $w=0.7$ , in which nuclei morphologies from left to right correspond to  $\mu=-3.05$ ,  $-3.08$ ,  $-3.10$ , and  $-3.18$ , respectively. The third row:  $w=0.5$ , in which nuclei morphologies from left to right correspond to  $\mu=-3.04$ ,  $-3.10$ ,  $-3.15$ , and  $-3.19$ , respectively. The last row:  $w=0.1$ , in which nuclei morphologies from left to right correspond to  $\mu=-2.94$ ,  $-2.95$ ,  $-2.96$ , and  $-2.97$ , respectively.

ues of the fluid-wall interaction ( $w=0.9, 0.7, 0.5, 0.3$ , and  $0.1$ ), and explored their corresponding nucleation behaviors. The typical shapes of critical nuclei at different chemical potentials are shown in Figs. 8 and 9, respectively, for capillary condensations and capillary evaporations.

For  $w=0.9$ , the morphologies of critical nuclei for evaporation and condensation are basically similar with those for  $w=2.5$ . However, there exist subtle differences between them. For the desorption process, when the chemical potential is near the liquidlike spinodal, the nucleus is apart from the wall and is of spherical shape. However as the chemical potential is close to capillary coexistence, the nucleus is also approximately spherical but come into contact with the pore walls partly (see the critical nuclei for  $\mu=-3.08$  and  $-3.10$  in Fig. 8 as examples). This observation is obviously different from the case of  $w=2.5$ , in which the critical nucleus at a high supersaturation states take the shape of ellipsoid and their long axis along the pore axis (see Fig. 6). We attribute the difference to the fact that the prewetting film only exists for strongly attractive fluid-wall  $w>0.9$ , but not for  $w=0.9$  or smaller (see Fig. 8).

For the capillary condensation, the morphologies of critical nuclei for  $w=0.9$  are in a shape of bridge at lower supersaturations and take a shape of annular bumps at higher supersaturations (see Fig. 9), also being different from in the case of  $w=2.5$  where the nucleation of capillary condensation always proceeds via the formation of annular bump. In

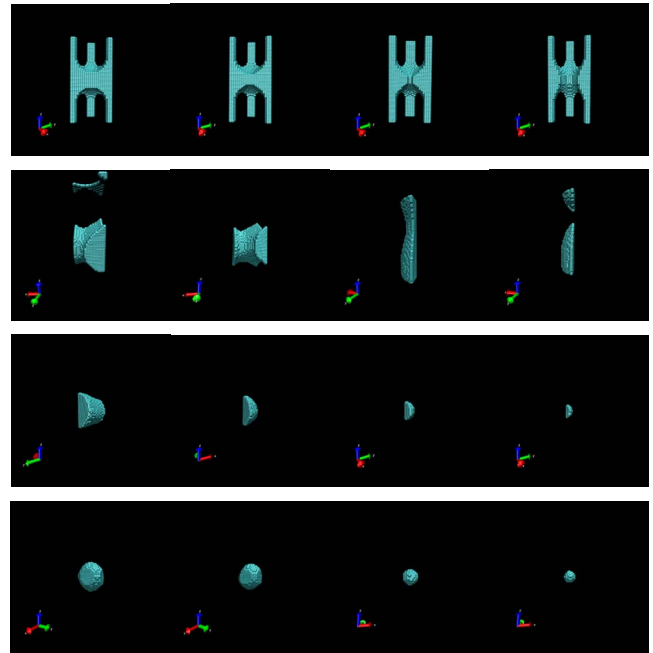


FIG. 9. (Color online) Morphologies of critical nuclei in adsorption branches for different  $w$ . The first row:  $w=0.9$ , in which nuclei morphologies from left to right correspond to  $\mu=-3.06$ ,  $-3.05$ ,  $-3.04$ , and  $-3.03$ , respectively. The second row:  $w=0.7$ , in which nuclei morphologies from left to right correspond to  $\mu=-3.02$ ,  $-3.00$ ,  $-2.98$ , and  $-2.96$ , respectively. The third row:  $w=0.5$ , in which nuclei morphologies from left to right correspond to  $\mu=-2.95$ ,  $-2.90$ ,  $-2.86$  and  $-2.81$ , respectively. The last row:  $w=0.1$ , in which nuclei morphologies from left to right correspond to  $\mu=-2.90$ ,  $-2.85$ ,  $-2.80$ , and  $-2.75$ , respectively.

the work of Kornev *et al.* [47], they suggested that the annular bump structures can be found for the critical nuclei at all supersaturations. While Husowitz and Talanquer [32] showed that the critical nuclei show a bridge structure at lower supersaturations and a bump structure at higher supersaturations. In this work, our calculations indicate that the difference can be interpreted by the strength of fluid-wall interaction. For the case of strong fluid-wall interaction, calculated results confirmed that the suggestion by Kornev *et al.* [47] holds. But when the fluid-wall interaction is moderate, the suggestion by Husowitz and Talanquer [32] holds. We contribute the difference to absence of the prewetting film which appears for  $w=2.5$ .

In general, the disappearance of the prewetting film has more significant effects on the nucleation of condensation than that of evaporation, as is shown in the nucleation barriers (see Fig. 10). By comparison of the nucleation barriers for  $w=2.5$  and  $w=0.9$ , it is found that as  $w$  decreases, the nucleation barrier for condensation increases substantially, while the nucleation barrier for evaporation is nearly kept fixed. As a result, the capillary coexistence moves to higher chemical potential, although in comparison with the bulk solution, the location of phase equilibrium for  $w=0.9$  shifts to lower chemical potential.

We then consider the case of  $w=0.7$ . Snapshots of critical nuclei in Figs. 8 and 9 show that the nucleation mechanisms for evaporation and condensation are both heterogeneous and

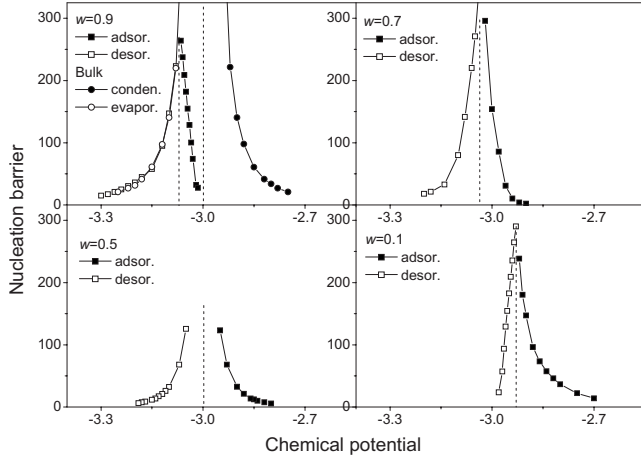


FIG. 10. Comparison of the nucleation barriers for pores with different  $w$ . The pore size is fixed at  $R_B=20$ . The dashed vertical lines correspond to the chemical potentials for the capillary coexistence, which is obtained from the adsorption isotherms [see Fig. 1(b)]. As a comparison, the nucleation barriers for bulk solution are also shown in the figure.

all the critical nuclei come into contact with pore walls. The contact angle of liquid droplet is found to be smaller than  $90^\circ$  while the contact angle of gas bubble is greater than  $90^\circ$ . This indicates the interaction between fluid-wall is still more favorable than fluid-fluid interaction. Note that the critical nucleus does not exhibit the geometrical symmetry of the pore. In comparison with  $w=0.9$ , the nucleation barrier for evaporation (see Fig. 10) in this case decreases and the nucleation barrier for condensation increases. Consequently, capillary coexistence moves to a higher chemical potential.

For  $w=0.5$ , both the shape of the critical nucleus and its nucleation barrier show a perfect symmetry between desorption and adsorption branches, as is shown in Figs. 8–10. For example, the curve of the nucleation barriers for condensation and that for evaporation are symmetrical about the capillary coexistence, very similar to the case of the bulk solution (see Fig. 10). Whereas the nucleation mechanism is heterogeneous in the pore with  $w=0.5$ , in contrast to homogeneous nucleation in the bulk solution. For the fluid-wall interaction of  $w=0.5$ , the critical nuclei, including bubbles for evaporation and droplets for condensation are both occur in a corner of the pore and appear in a quarter-sphere shape. In other words, the contact angle is  $90^\circ$ . Thus, the location of capillary coexistence is identical to that for the phase transition in bulk solution, although the nucleation barrier is much lower than that for the bulk solution.

When the fluid-wall interaction decreases to  $w=0.3$ ,  $w=0.1$ , and then  $w<0.1$ , the critical nuclei for desorption and those for adsorption was also studied. The results for  $w=0.1$  are shown in Figs. 8 and 9, respectively. For  $w<0.5$ , such as  $w=0.3$ , the critical droplet formed in a corner of the pore tends to detach from the wall (with contact angle less than  $90^\circ$ ) due to the poorly wetted surface. As  $w$  decrease to  $w=0.1$  or smaller, the critical droplet is of spherical shape and locates in the center of the pore, as shown in Fig. 9. For the nucleation of capillary evaporation, the critical bubble for  $w<0.5$  is prone to attach the wall (with contact angle greater

than  $90^\circ$ ), and finally for  $w=0.1$  or smaller, evaporation is induced by nucleation of bubbles in a bridge shape at high supersaturation states, and in the shape of annular bump at low supersaturation states (see Fig. 8). In comparison with the phase transition in the bulk solution, our results demonstrate that the weak attraction due to the pore wall causes the nucleation mechanism for capillary evaporation changing from homogeneous to heterogeneous nucleation (see Fig. 8). The heterogeneous nucleation near the wall reduces the nucleation barrier substantially (see Fig. 10) and makes the evaporation take place at the lower chemical potentials [48]. At the same time, the nucleation behavior for capillary condensation is nearly identical to that for bulk solution. Hence, the equilibrium phase transition shifts to higher chemical potential.

By examining the calculation results for different fluid-wall interactions, it can be concluded that  $w=0.5$  is a particular value. For the case  $w=0.5$ , the nucleation behaviors for condensation and evaporation are symmetrical. This agrees with the suggestion by Kierlik *et al.* [40] that there is symmetry  $w \leftrightarrow 1-w$  for the model we used. Since the fluid-wall interaction  $w$  denotes the “wettability” of the wall. It influences on the contact angle, and thus the geometry of the nuclei. If the fluid-wall interaction  $w$  is greater than 0.5, the droplet preferably spreads on the wall and the bubble tend to detach from the wall. On the contrary, if the fluid-wall interaction  $w$  is less than 0.5, the droplet tends to detach from the wall and the bubble is preferable to form near the wall.

#### IV. CONCLUSIONS

In this work, we modified the classical density functional theory method to stabilize a nucleus by imposing a suitable constraint, hence the shape and structure of nuclei can be directly calculated without using a predefined nucleus as input. With this technique, we investigated the effects of fluid-wall interaction on the nucleation mechanisms for vapor-liquid phase transitions in the confined systems and related the nature of hysteresis to the nucleation mechanisms.

First, we studied adsorption isotherms of simple fluids in square-shaped nanopores with the width of  $R_B=20$  and infinite length. It is found from adsorption isotherms that the chemical potentials for the liquidlike spinodals are nearly identical for the different pore sizes and different liquid-wall interaction parameters,  $w$ , as long as  $w>0.9$ . Moreover, the chemical potentials agree with that for the bulk liquid spinodal. While for  $w$  is small enough ( $w<0.1$ ), the positions of the vaporlike spinodals take place at the same chemical potential as that for the bulk liquid spinodal, regardless of the pore width and the fluid-wall interaction. According to the characteristics of the adsorption isotherms, in this work we have classified  $w$  into three regions, which are denoted as strongly ( $w>0.9$ ), weakly ( $0 \leq w < 0.1$ ), and moderately ( $0.1 \leq w \leq 0.9$ ) attractive fluid-wall interaction regions, respectively.

Then we attempted to interpret the adsorption characteristics in terms of the nucleation mechanism. For the nucleation of evaporation in the confined system with strongly attractive fluid-wall interactions, our calculations indicate

that it is easier for the nucleated spherical bubble to generate in the center of the pore rather than in the other places. Since small nuclei in the center of the pore are not affected significantly by the wall, the homogeneous nucleation of evaporation for the case of  $w > 0.9$  behaves as that in the bulk. This observation can be used to explain why the liquidlike spinodals, which are identical for the systems with different  $w$  values in the range of  $w > 0.9$  and different pore sizes, take the same positions as that for the bulk liquid-to-vapor transition.

For the systems of  $w > 0.9$ , the strong attraction from the pore wall changes the nucleation mechanism of the capillary condensation. Our calculations demonstrate that the condensation originates from nucleation of annular bumps near the pore wall, rather than homogeneous nucleation in the pore center. The nucleation barrier is found to be substantially lower than that for the homogeneous nucleation, which thus shifts the liquidlike spinodal and also capillary coexistence to a lower chemical potential. In general, our results confirm that hysteresis of confined fluids originates from the difficulty of nucleation of the new phase. The deviation of the nucleation mechanism from that of bulk solution would substantially decrease the nucleation barrier, which shifts the equilibrium phase transition and shrinks the width of the hysteresis loop against its bulk counterpart.

For the situation with the weakly attractive fluid-wall interaction ( $w < 0.1$ ), our calculations show that the nucleation of condensation is nearly the same as that in the bulk solution, i.e., homogeneous nucleation. In contrast, the evaporation transition originates from the nucleation of bubbles in the shape of annular bump or bridge near the wall, which reduces the nucleation barriers. It is the unfavorable fluid-wall interaction that alters the nucleation mechanism of capillary evaporation, which shifts the liquidlike spinodal and capillary coexistence to a higher chemical potential.

When the pore is of the moderately attractive fluid-wall interaction ( $0.1 \leq w \leq 0.9$ ), the nucleation mechanism can be heterogeneous for both the condensation and evaporation transitions. Again, the heterogeneous nucleation reduces the nucleation barrier for the nucleation of the new phase, and changes the position and width of hysteresis against its bulk counterpart. In general  $w=0.5$  is a particular value, at which the nucleation behaviors for condensation and evaporation are symmetrical. If the fluid-wall interaction  $w$  is greater than 0.5, the nucleation of capillary condensation are more significantly affected than that of capillary evaporation, and the droplet preferably spreads on the wall and the bubble tend to detach from the wall. On the contrary, if the fluid-wall interaction  $w$  is less than 0.5, the nucleation of capillary evaporation are more significantly affected than that of capillary condensation, and the droplet tends to detach from the wall and the bubble is preferable to form near the wall.

In this work, we also reveal that the calculated critical nucleus may show a transition path dependence, especially for nucleation of condensation for  $w > 0.5$  and nucleation of evaporation for  $w < 0.5$ . By taking into account of the transition path dependence, it is found that for strong fluid-wall interaction ( $w > 0.9$ ), the critical nuclei of capillary condensations always take the shape of bump. While for moderate fluid-wall interaction both bump and bridge structures are possible, depending on the supersaturation.

#### ACKNOWLEDGMENTS

The work was supported by National Natural Science Foundation of China (Grants No. 20736005 and No. 20876004). X.Z. acknowledges the support of the Research Foundation for Young Researchers of BUCT. Generous allocations of computer time by "Chemical Grid Project" of BUCT, and the Supercomputing Center, CNIC, CAS are acknowledged.

- 
- [1] P. G. Debenedetti, *Metastable Liquids: Concepts and Principles* (Princeton University Press, Princeton, NJ, 1996).
  - [2] D. W. Oxtoby and R. Evans, *J. Chem. Phys.* **89**, 7521 (1988).
  - [3] X. C. Zeng and D. W. Oxtoby, *J. Chem. Phys.* **94**, 4472 (1991).
  - [4] F. Trudu, D. Donadio, and M. Parrinello, *Phys. Rev. Lett.* **97**, 105701 (2006).
  - [5] S. Auer and D. Frenkel, *Nature (London)* **409**, 1020 (2001).
  - [6] M. J. Uline and D. S. Corti, *Phys. Rev. Lett.* **99**, 076102 (2007).
  - [7] V. Talanquer, *J. Chem. Phys.* **122**, 084704 (2005).
  - [8] S. Auer and D. Frenkel, *Phys. Rev. Lett.* **91**, 015703 (2003).
  - [9] S. Auer and D. Frenkel, *J. Chem. Phys.* **120**, 3015 (2004).
  - [10] P. A. Apte and I. Kusaka, *J. Chem. Phys.* **121**, 12532 (2004).
  - [11] V. K. Shen and P. G. Debenedetti, *J. Chem. Phys.* **111**, 3581 (1999).
  - [12] V. K. Shen and P. G. Debenedetti, *J. Chem. Phys.* **114**, 4149 (2001).
  - [13] A. Cacciuto, S. Auer, and D. Frenkel, *Phys. Rev. Lett.* **93**, 166105 (2004).
  - [14] K. Laasonen, S. Wonzak, R. Strey, and A. Laaksonen, *J. Chem. Phys.* **113**, 9741 (2000).
  - [15] K. Yasuoka and X. C. Zeng, *J. Chem. Phys.* **126**, 124320 (2007).
  - [16] Z. Li and J. Wu, *Ind. Eng. Chem. Res.* **47**, 4988 (2008).
  - [17] A. V. Neimark and A. Vishnyakov, *J. Chem. Phys.* **122**, 054707 (2005).
  - [18] D. H. Everett and J. M. Haynes, *J. Colloid Interface Sci.* **38**, 125 (1972).
  - [19] L. D. Gelb, K. E. Gubbins, R. Radhakrishnan, and M. Sliwinska-Bartkowiak, *Rep. Prog. Phys.* **62**, 1573 (1999).
  - [20] U. M. B. Marconi and F. van Swol, *Europhys. Lett.* **8**, 531 (1989).
  - [21] U. M. Marconi and F. Van Swol, *Phys. Rev. A* **39**, 4109 (1989).
  - [22] P. Kowalczyk, K. Kaneko, L. Solarz, A. P. Terzyk, H. Tanaka, and R. Hołyst, *Langmuir* **21**, 6613 (2005).
  - [23] B. Coasne, A. Grosman, C. Ortega, and M. Simon, *Phys. Rev. Lett.* **88**, 256102 (2002).
  - [24] P. A. Monson, *Langmuir* **24**, 12295 (2008).

- [25] P. A. Monson, *J. Chem. Phys.* **128**, 084701 (2008).
- [26] A. Bah, N. Dupont-Pavlovsky, and X. Duval, *Surf. Sci.* **352–354**, 518 (1996).
- [27] A. J. Page and R. P. Sear, *Phys. Rev. Lett.* **97**, 065701 (2006).
- [28] A. Vishnyakov and A. V. Neimark, *J. Chem. Phys.* **119**, 9755 (2003).
- [29] A. V. Neimark, P. I. Ravikovitch, and A. Vishnyakov, *Phys. Rev. E* **65**, 031505 (2002).
- [30] A. V. Neimark and A. Vishnyakov, *J. Phys. Chem. B* **110**, 9403 (2006).
- [31] V. Talanquer and D. W. Oxtoby, *J. Chem. Phys.* **114**, 2793 (2001).
- [32] B. Husowitz and V. Talanquer, *J. Chem. Phys.* **121**, 8021 (2004).
- [33] H. J. Woo, F. Porcheron, and P. A. Monson, *Langmuir* **20**, 4743 (2004).
- [34] E. A. Ustinov and D. D. Do, *J. Phys. Chem. B* **109**, 11653 (2005).
- [35] P. G. Bolhuis and D. Chandler, *J. Chem. Phys.* **113**, 8154 (2000).
- [36] P. G. Bolhuis, D. Chandler, C. Dellago, and P. L. Geissler, *Annu. Rev. Phys. Chem.* **53**, 291 (2002).
- [37] C. Dellago, P. G. Bolhuis, and P. L. Geissler, *Adv. Chem. Phys.* **123**, 1 (2002).
- [38] J. Wedekind, D. Reguera, and R. Strey, *J. Chem. Phys.* **125**, 214505 (2006).
- [39] E. Kierlik, P. A. Monson, M. L. Rosinberg, L. Sarkisov, and G. Tarjus, *Phys. Rev. Lett.* **87**, 055701 (2001).
- [40] E. Kierlik, P. A. Monson, M. L. Rosinberg, and G. Tarjus, *J. Phys.: Condens. Matter* **14**, 9295 (2002).
- [41] F. Porcheron and P. A. Monson, *Langmuir* **20**, 6482 (2004).
- [42] L. Sarkisov and P. A. Monson, *Phys. Rev. E* **65**, 011202 (2001).
- [43] X. Zhang, D. Cao, and W. Wang, *J. Chem. Phys.* **119**, 12586 (2003).
- [44] X. Zhang and W. Wang, *Phys. Rev. E* **74**, 062601 (2006).
- [45] X. Zhang, D. Cao, and W. Wang, *J. Colloid Interface Sci.* **308**, 49 (2007).
- [46] Z. Feng, X. Zhang, and W. Wang, *Phys. Rev. E* **77**, 051603 (2008).
- [47] K. G. Kornev, I. K. Shingareva, and A. Vishnyakov, *Adv. Colloid Interface Sci.* **96**, 143 (2002).
- [48] K. Lum, D. Chandler, and J. D. Weeks, *J. Phys. Chem. B* **103**, 4570 (1999).